Supplementary Information

Bioinspired Dual-Modal Laser-Induced Graphene Tactile Sensor for High-Precision Multimodal Object Recognition

*Gongmo Xiang,[a] Guozhen Zhang,[c] Guoning Yin,[a] Zhenya Ge,[a] Weijie Wang,[a] Lingyun Xu,[a] and Xiangyu Jiang[b,]**

[a]School of Chemistry, Beihang University, Beijing 100191, P.R. China

[b]International Research Institute for Multidisciplinary Science, Beihang University, Beijing 100191, P.R. China

[c]School of Cybersecurity, Northwestern Polytechnical University, Xi'an 710072, P.R. China

*Corresponding authors

E-mail address: jiangxy@buaa.edu.cn (X. Jiang)

1.Materials

PI film (500HN) was purchased from DuPont, anhydrous ethanol (GR, 500 mL) was purchased from Sinopharm Chemical Reagent Co., Ltd., and 3M tape (3M4905VHB) was purchased from 3M.

2.Characterization and measurement

SEM images were obtained using a field emission gun scanning electron microscope (FEI, QUANTA FEG 250, USA) at an accelerating voltage of 10 kV. Raman spectra were collected using a high-resolution Raman spectrometer (Horiba, LabRam HR Evolution, Japan) with an excitation wavelength of 532 nm. The full spectrum and C1s, N1s, and O1s fine spectra of RLIGF and PI films were obtained using an X-ray photoelectron spectrometer (ThermoFisher Scientific, ESCALAB 250Xi, UK). The square resistance of RLIGF was measured using a four-probe tester (4 Probes Tech Ltd, RTS-8, China), with each sample measured five times. An optical microscopy image of the rough substrate was obtained using a fluorescence microscope (Olympus, BX53, Japan). The electrical output properties (voltage, resistance), bending tensile test, and 1500-cycle stability test of BTTS were tested and recorded using a Keithley 6514 electrometer, Keithley 2400 and a servo computer-type push-pull tester (TOPHUNG, TH-8203S, China).

3.Fabrication of BTTS

A PI film was soaked in anhydrous ethanol and ultrasonically cleaned for 5 min, then rinsed with deionized water three times. A 10.6 μm CO_2 laser marking machine (Kerui Laser, KRDB CO_2 30W, China) was used to convert the cleaned PI film into RLIGF. The laser mode was set to grating mode, with a laser power of 10.5 W, a speed of 500 mm/s, and a frequency of 1000 Hz. Line spacings of 100, 125, 150, 175, and 200 μm were used for the first irradiation to prepare rough substrates with different microstructures. RLIGF was prepared based on the rough substrate. The laser power was set to 19.5 W, the speed to 500 mm/s, the frequency to 3000 Hz, and the line spacing to 150 μm. The rough substrate was subjected to secondary irradiation to obtain RLIGF. The size of all RLIGFs was designed to be 10 mm × 20 mm. A 3M tape with a width of 5 mm was adhered around the RLIGF to form a BTTS.

4.Electrical simulation

The model was constructed using COMSOL Multiphysics (version 6.2, Sweden) and imported via the AC/DC module. The upper layer of the model was composed of PI, and the lower layer was composed of RLIGF. By applying surface charge density and suspension potential to the upper and lower surfaces, the potential distribution and potential difference between the two friction layers were simulated for comparative analysis. The surface charge density and suspension potential were measured using a Keithley 6514 electrometer.

5.Establishment of a dataset for object recognition

The dataset of triboelectric and piezoresistive signals for identifying eight objects was established based on data obtained by wearing BWWS and grasping each object continuously no fewer than 500 times: banana, paper box, glass cup, tennis ball, plastic bottle, hand, leather cover, and ceramic bowl.

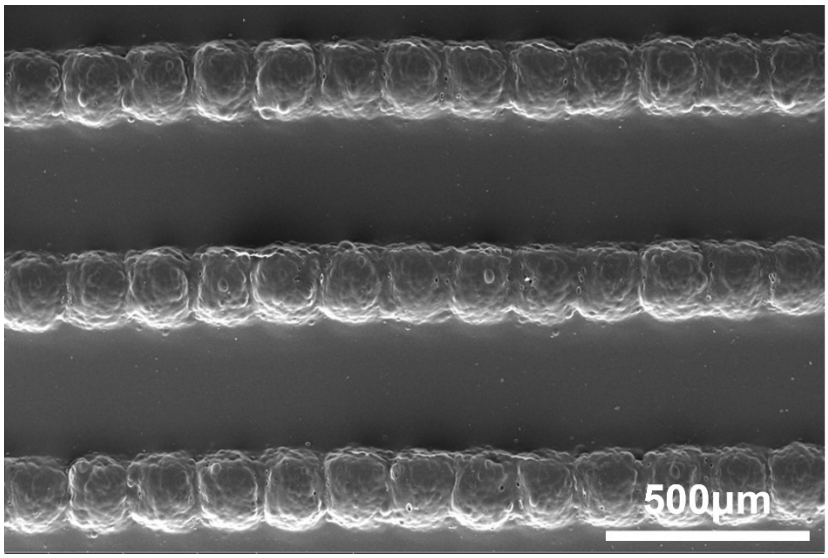

Figure. S1. The SEM photo of first irradiated PI film.

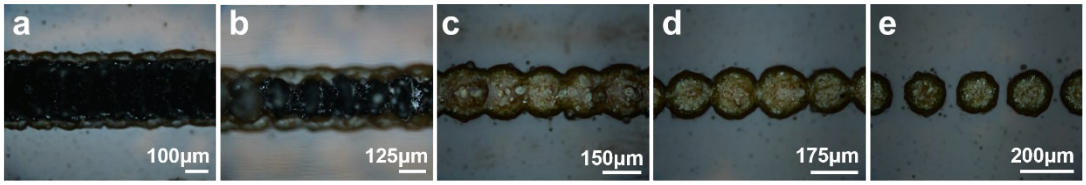

Figure. S2. Optical microscope images of the first laser-irradiated PI film at different line spacings: (a) 100 μm, (b) 125 μm, (c) 150 μm, (d) 175 μm, and (e) 200 μm. When the line spacing is not greater than 125 μm, the rough array surface is carbonized. As the line spacing increases further, the rough array gradually changes from a continuous line array to a discrete point array.

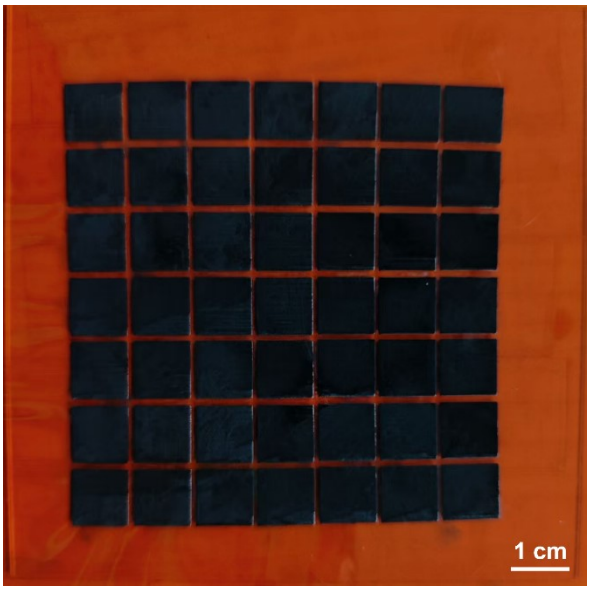

Figure S3. A 7 × 7 RLIGF array fabricated on a PI film.

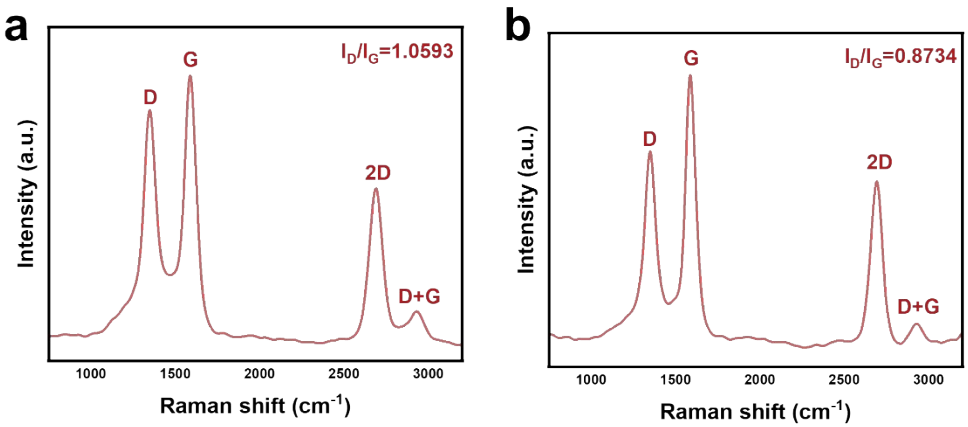

Figure. S4. Raman spectra of RLIGF under different secondary irradiation powers: (a) 16.5 W and (b) 22.5 W. The I_D/I_G values are 1.0593 and 0.8734, respectively. The RLIGF samples prepared under different laser powers all exhibited the three characteristic peaks of graphene. Moreover, with increasing laser power, the I_D/I_G ratio of RLIGF gradually decreased, indicating a reduction in defect density and an enhancement in the degree of graphitization

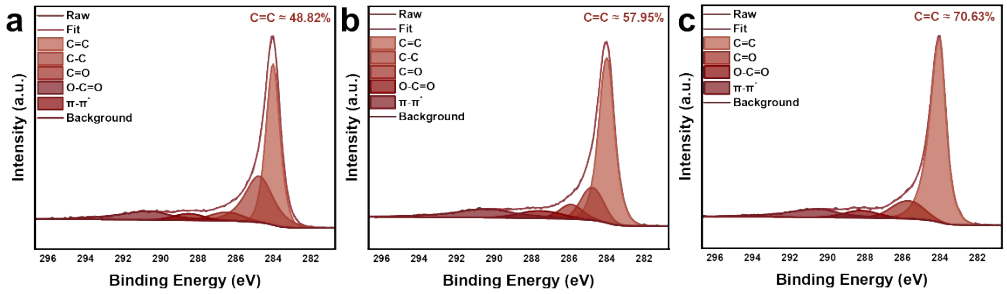

Figure. S5. XPS C1s spectra of RLIGF at different secondary irradiation powers: (a) 16.5 W, (b) 19.5 W, and (c) 22.5 W. With increasing laser power, the content of C=C increases from 48.82% to 70.63%.

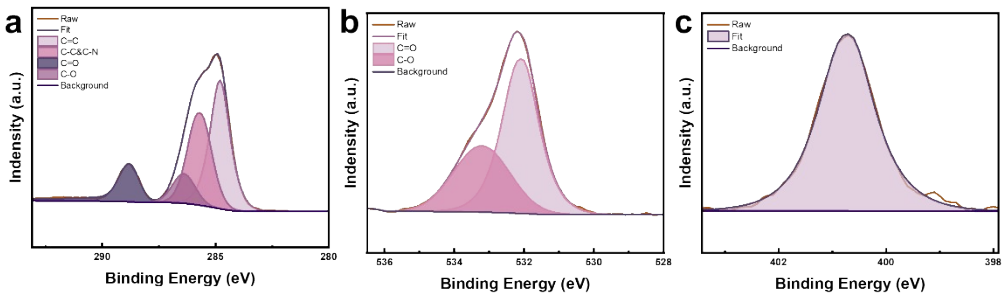

Figure. S6. XPS spectra of PI film: (a) C1s, (b) O1s, and (c) N1s.

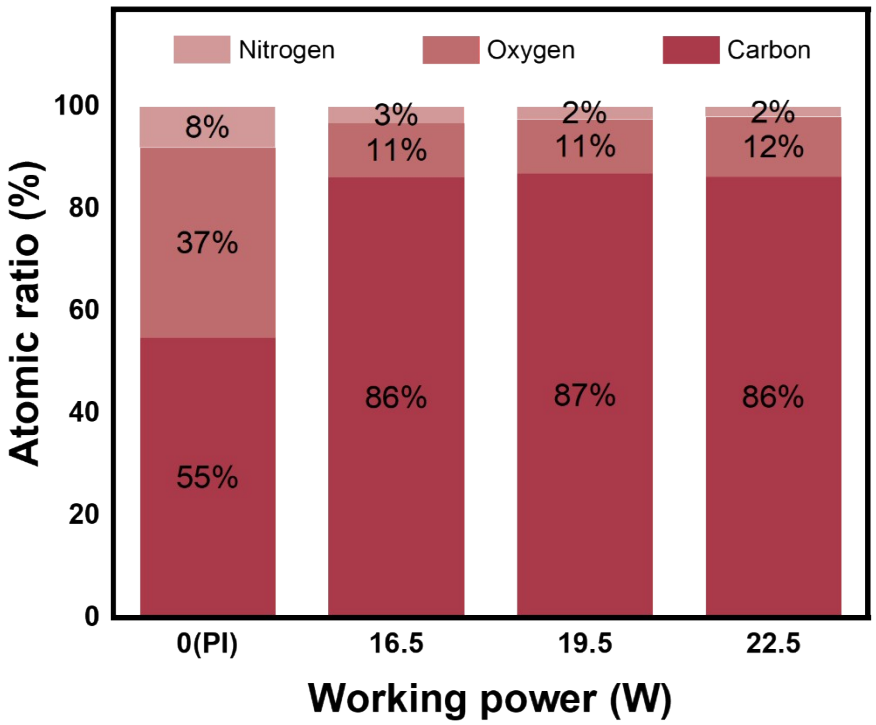

Figure. S7. Comparison of C, N, and O contents of RLIGF and PI films under different secondary irradiation powers. The elemental compositions (C, N, and O) of the three RLIGF samples exhibit a significant increase in C content, accompanied by a decrease in N and O contents.

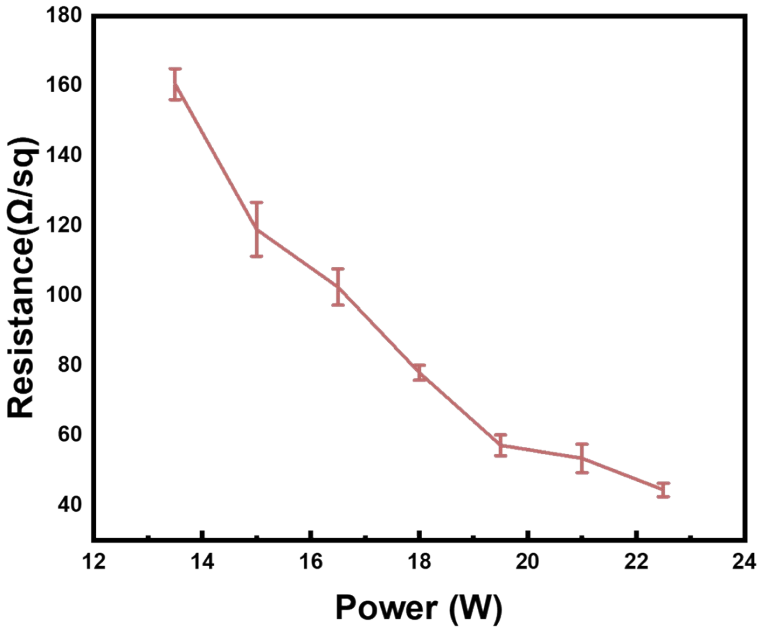

Figure. S8. Square resistance of RLIGF under different secondary irradiation powers. The square resistance of RLIGF decreases with increasing irradiation power.

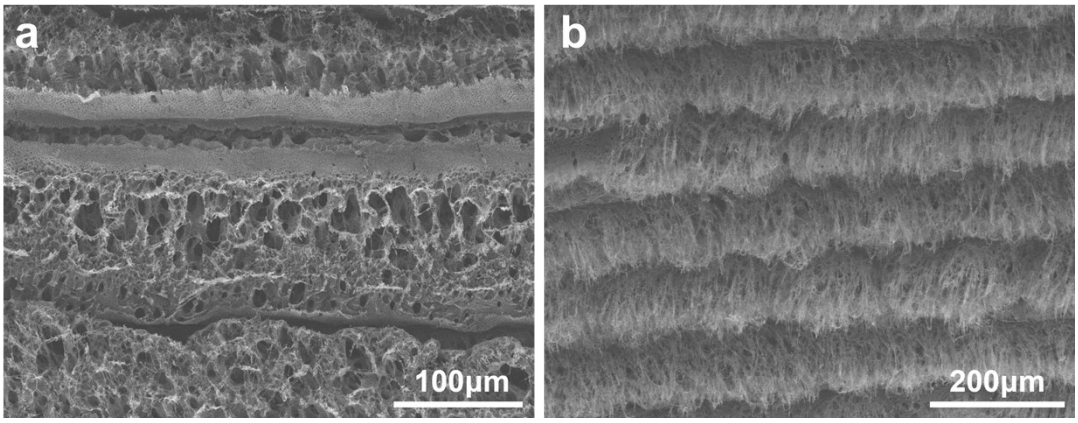

Figure. S9. The SEM photo of (a) LIG and (b) LIGF.

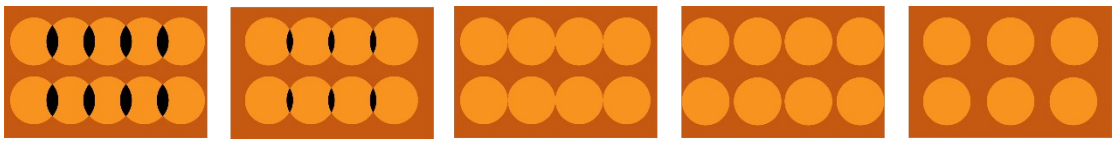

Figure. S10. Schematic diagram illustrating the effect of the line spacing of the first irradiation on the output performance of BTTS. Too small a line spacing causes carbonization of the overlapping area of the light spots, preventing the formation of the fiber structure after the second irradiation. When the line spacing between the light spots is continuous and not carbonized, it represents a critical state. The RLIGF obtained in this state exhibits continuous and dense LIGF1, with the highest density of rough bumps. A further increase in line spacing leads to spot separation, reducing the density of rough bumps per unit area and increasing the content of LIGF2 grown on the flat PI surface, which plays a major role in the resistance change caused by strain.

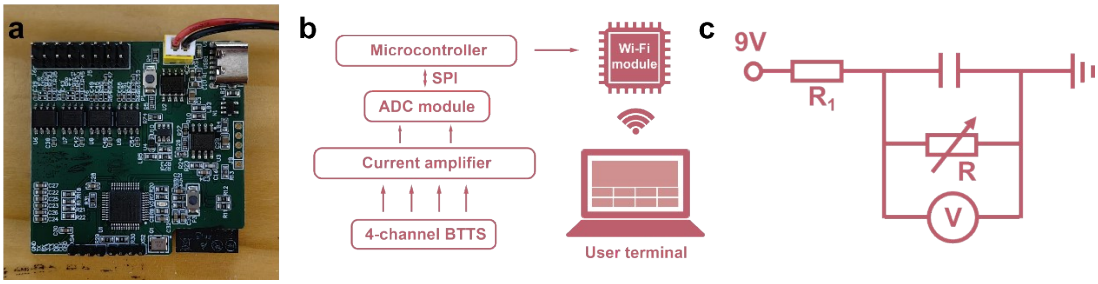

Figure. S11. (a) Image of the signal acquisition circuit board (b) flowchart of the data collection and transmission process of the signal acquisition circuit board and (c) equivalent circuit diagram for signal acquisition. The acquisition of electrical signals is primarily based on a wireless 8-channel integrated circuit. This circuit is designed using Altium Designer 18 and comprises a power management module, an analog-to-digital conversion (ADC) module, a dual-channel pre-current amplifier, a Wi-Fi module (ESP32), and a main control module (STM32). The pre-current amplifier accurately collects and amplifies sensor signals before transmitting them to the ADC chip for digitization. Under precise program control by the main control chip, the SPI protocol enables continuous and real-time signal acquisition, achieving a sampling rate of up to 1 kS/s per channel, supporting 8-channel parallel acquisition. Subsequently, the digitized multi-channel data is wirelessly transmitted to the mobile receiving terminal via the ESP32 communication module using the UDP protocol. Finally, with the assistance of LabVIEW-based custom computer programs, real-time reception, visualization, and efficient storage of multi-channel data are achieved.

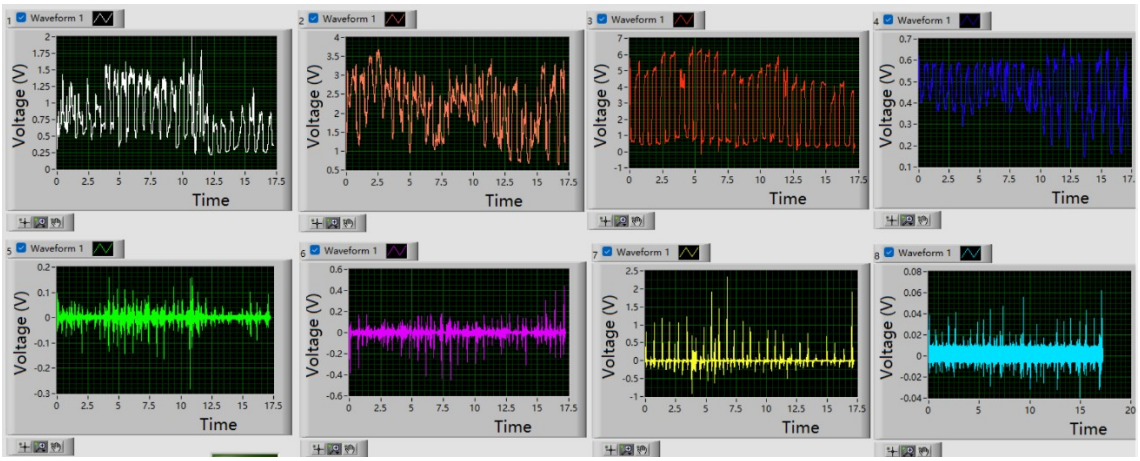

Figure. S12. Multi-channel sensor signals displayed on the user terminal. The first row presents the resistance variations of BTTS across different channels, while the second row illustrates the triboelectric voltage variations of BTTS across different channels.

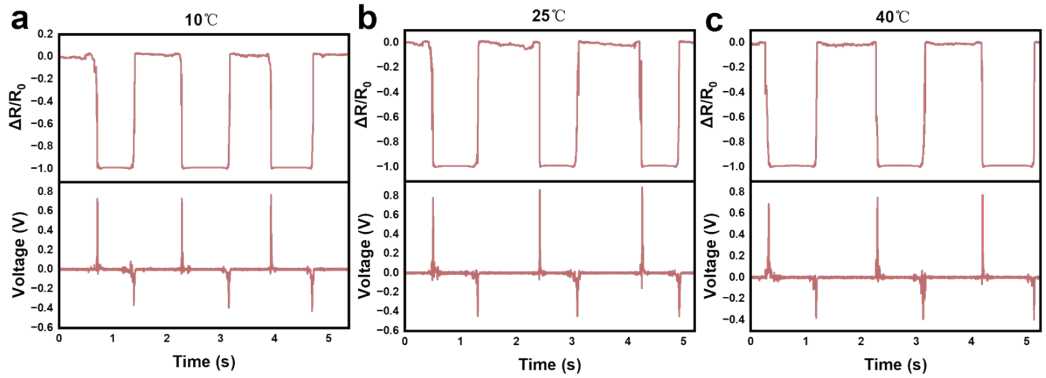

Figure. S13. Sensing signals of wearing BTTS at (a) 10 ℃, (b) 25 ℃ and (c) 40 ℃

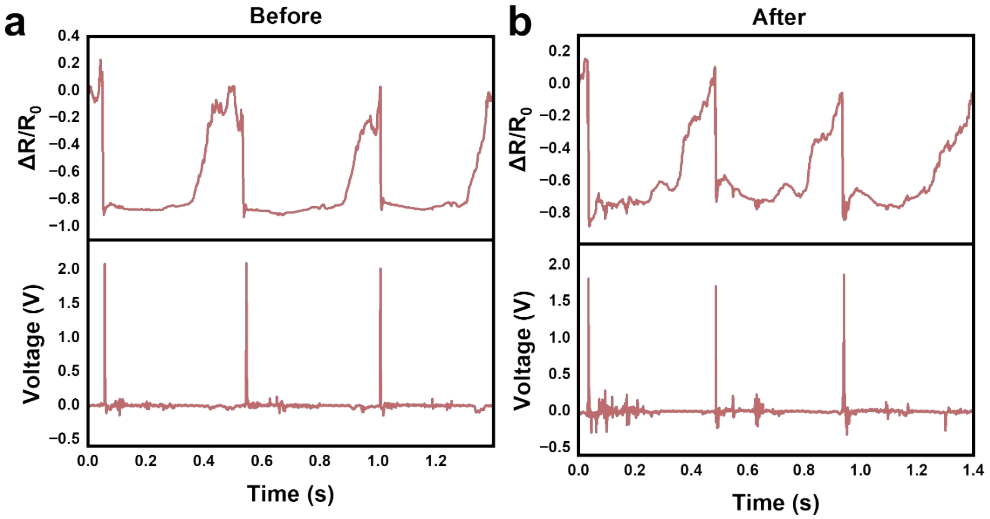

Figure. S14. Stability of BTTS sensing performance after repeated grasping cycles. (a) sensing signals of BTTS before repeated grasping. (b) sensing signals of BTTS after >5000 repeated grasping cycles.

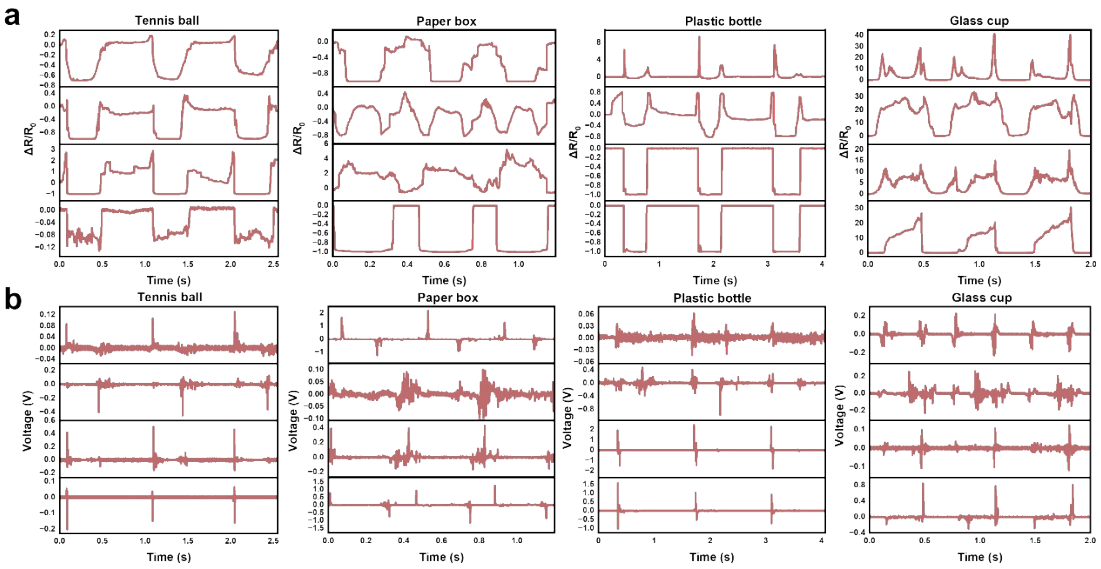

Figure. S15. (a) Four-channel piezoresistive sensing signals for shape recognition from the remaining four objects using BWWS. (b) Four-channel triboelectric sensing signals for material recognition from the remaining four objects using BWWS.

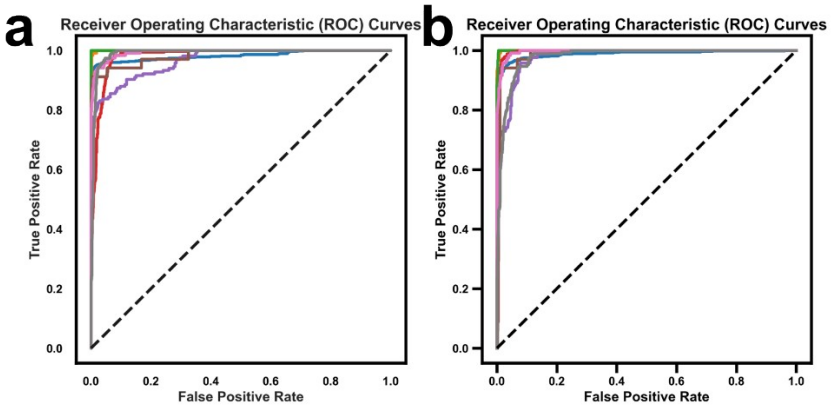

Figure. S16. ROC curves of (a) triboelectric and (b) piezoresistive signals, with corresponding AUCs of 0.9876 for triboelectric signal and 0.9913 for piezoresistive signal.

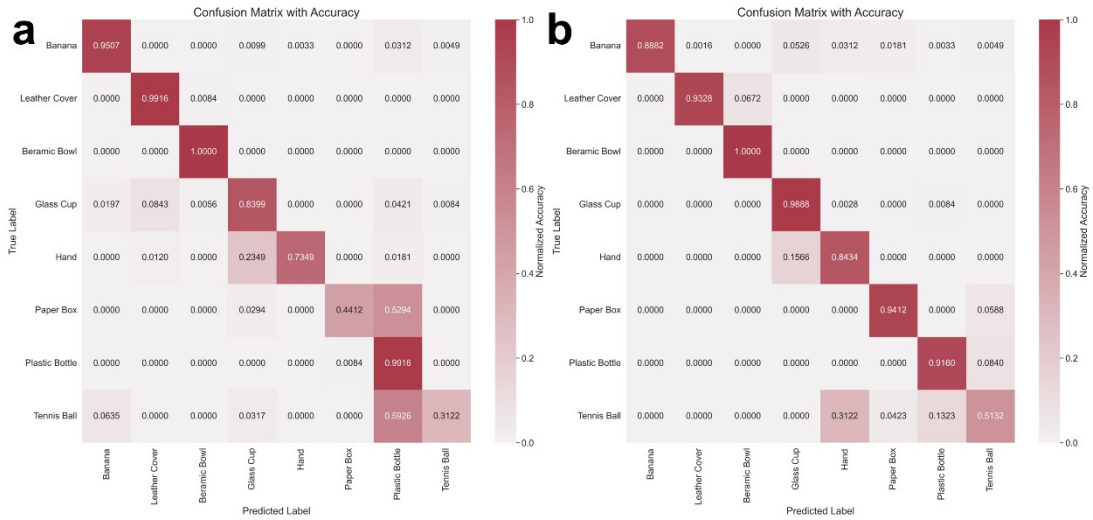

Figure. S17. Confusion matrices of (a) the single triboelectric signal (accuracy: 83.7%) and (b) the single piezoresistive signal (accuracy: 87.7%).

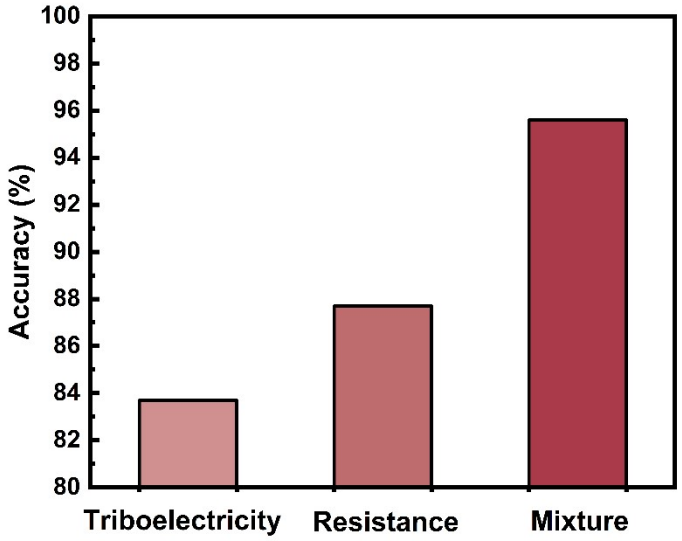

Figure. S18. Comparison of recognition accuracy under different sensor signals, with accuracies of 83.7%, 87.7% and 95.6% respectively.

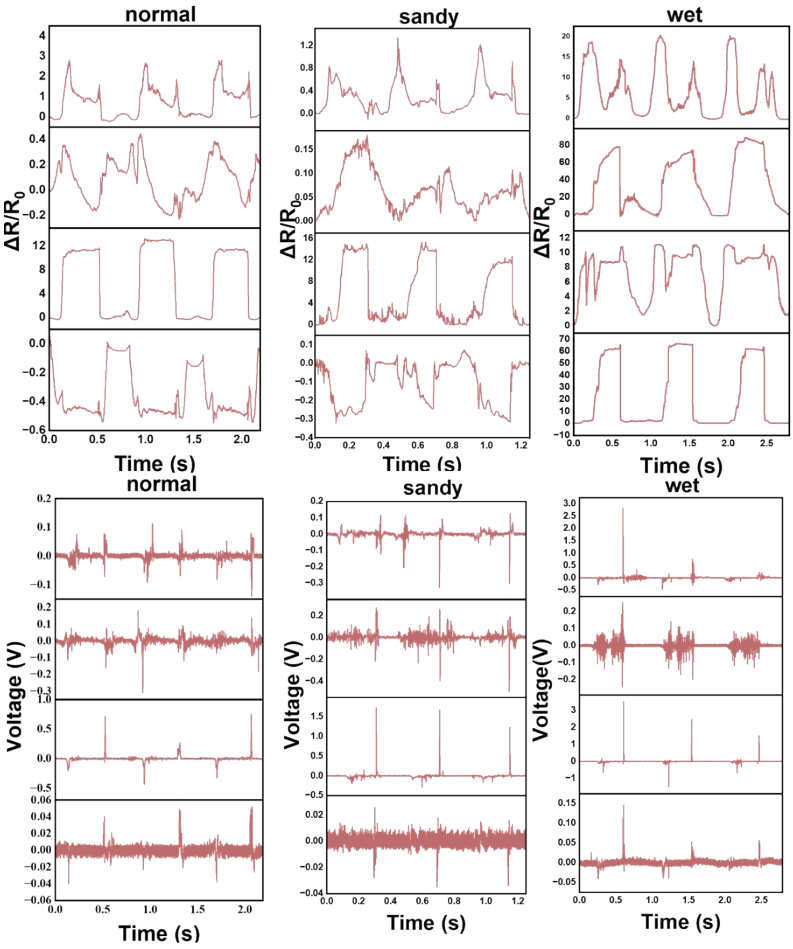

Figure. S19. The multi-channel sensing signals when wearing BWWS to grasp objects in normal, sandy, and wet states.

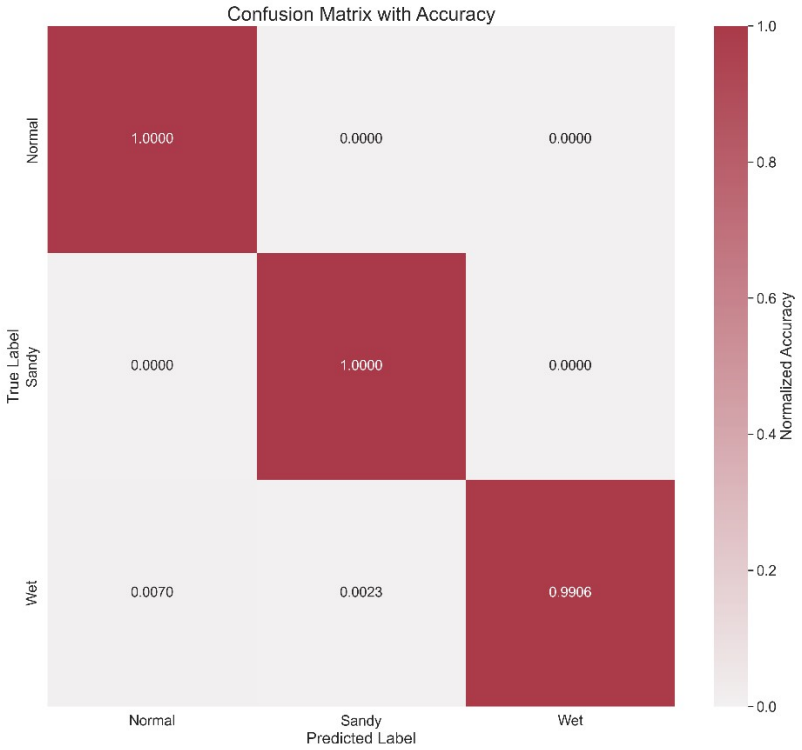

Figure. S20. Confusion matrix for object recognition in different states (normal, sandy and wet). The recognition accuracy of objects in various states approaches 100%.

	Cost (size)	Cost per sensor	Total cost per sensor
PI film	300 CNY (A4)	0.96 CNY	0.98 CNY
Tape	3.88 CNY (3m)	0.02 CNY	

Table S1. Raw material cost for BTTS fabrication; the material cost of a single BTTS is only 0.98 CNY

Materials	Working mechanism	Haptic mode		Number of Sensors	AI processing		Ref
		Material type	Material shape		Method	Accuracy	
RLIGF	Triboelectric/ Resistance	√	√	4	CNN	95.6%	This work
Ionogel yarn/Aramid fiber/Silicone	Triboelectric	N/A	√	5	SVM	90.38%	[1]
PI/PDMS/Cr/Pt/CAM	N/A	√	√	10	MLP	94%	[2]
MWCNTs/PDMS/Ecoflex/Cu	Capacitance	N/A	√	2	sing-ANN KNN	92.6% 93.1%	[3]
AgNW/Ecoflex sponge	Triboelectric	√	N/A	2	Regression model	93.3%	[4]
AgNW/rGo/PDMS	Resistance	√	N/A	1	SVM	55%	[5]
Melamine sponge/ PEDOT:PSS	Piezoresistance/ Thermoelectricity	√	N/A	1	Decision tree	94.7%	[6]

Table S2. Comparison of object recognition techniques in other tactile sensors. Recognition accuracies are reported as described in the respective literature and are provided for reference-level comparison, as datasets and experimental protocols vary across studies.

Movie S1. Wireless real-time object sensing via BWWS.

References

1 X. Zhong, P. Sun, R. Wei, H. Dong and S. Jiang, *J Mater Chem A Mater*, 2022, 10, 15080–15088.

2 G. Li, S. Liu, L. Wang and R. Zhu, *Sci Robot*, 2020, 5, eabc8134.

3 B. Xu, D. Chen, Y. Wang, R. Tang, L. Yang, H. Feng, Y. Liu, Z. Wang, F. Wang and T. Zhang, *Adv Electron Mater*, 2023, 9, 2201334.

4 D. Zhu, J. Lu, M. Zheng, D. Wang, J. Wang, Y. Liu, X. Wang and M. Zhang, *Nano Energy*, 2023, 114, 108644.

5 W. Lin, Z. Wang, Y. Xu, Z. Hu, W. Zhao, Z. Zhu, Z. Sun, G. Wang and Z. Peng, *Advanced Materials*, 2024, 36, 2305032.

6 Y. Li, L. Yang, S. Deng, H. Huang, Y. Wang, Z. Xiong, S. Feng, S. Wang, T. Li and T. Zhang, *InfoMat*, 2023, 5, e12463.